Cronfa - Swansea University Open Access Repository

Paper:

Accepted Manuscript

Metamodel-based approach for stochastic free vibration analysis of functionally graded carbon nanotube reinforced plates

Enrique García-Macías, Rafael Castro-Triguero, Michael I. Friswell, Sondipon Adhikari, Andrés Sáez

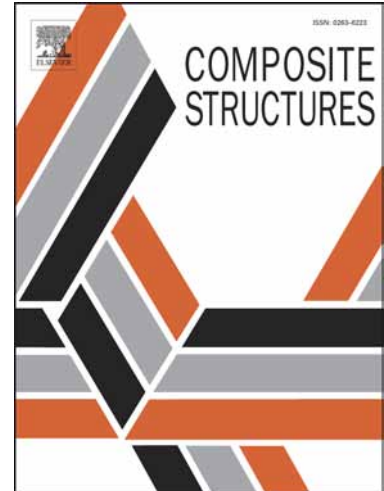# Metamodel-based approach for stochastic free vibration analysis of functionally graded carbon nanotube reinforced plates.

Enrique García-Macías[a,*], Rafael Castro-Triguero[b], Michael I. Friswell[c], Sondipon Adhikari[c], Andrés Sáez[a]

[a]*Department of Continuum Mechanics and Structural Analysis, School of Engineering, University of Seville , Camino de los Descubrimientos s/n, E-41092-Seville, Spain*
[b]*Department of Mechanics, University of Cordoba, Campus de Rabanales, Cordoba, CP 14071, Spain*
[c]*Zienkiewicz Centre for Computational Engineering, College of Engineering, Swansea University, Singleton Park, SA2 8PP, United Kingdom*

Highlights

- The CNT distribution and material parameters considered as a sources of uncertainty.

- Power-law and truncated Gaussian functions to define CNT variability along thickness.

- Kriging and RS-HDMR are employed as surrogate models.

Abstract

The remarkable mechanical and sensing properties of carbon nanotubes (CNTs) suggest that they are ideal candidates for high performance and self-sensing cementitious composites. However, there is still a lack of deeper knowledge of the uncertainty associated with their incorporation into functionally graded composite materials (FGM). The influence of these uncertainties can be critical for future applications in the field of Structural Health Monitoring (SHM), techniques that usually require high accuracy modeling. Most researchers restrict the aim of their studies to the analysis of composite materials with uniform or linear grading profiles. This study sheds new light on the basis of stochastic representation of the grading profiles and analyzes the propagation of its uncertainty into the response of FG-CNT reinforced plates. The finite element method (FEM) is employed to study the individual and interactive effects of the mechanical properties (matrix/CNTs) and grading profiles via power-law distributions. The effects of stochastic uncertainties on the overall properties of the composite material are represented using probability theory.

1. Introduction

Since the discovery of carbon nanotubes (CNTs) by Ijima [1] in 1991, many researchers have investigated their unique capabilities as reinforcements in composite materials (CNTRC). Due to their remarkable mechanical, electrical and thermal properties, carbon nanotubes are considered as ideal reinforcing fibers for advanced high strength materials and smart materials with self-sensing capabilities [2, 3]. These features are specially interesting in the field of Structural Health Monitoring (SHM). The correlation between the variation of the applied stresses with the electrical resistance leads to infinite possibilities for the control and assessment of civil structures. Although still in initial development phases, these capabilities have already been demonstrated experimentally [4–8]. Another promising direction is the application of CNTs as reinforcements in functionally graded materials (FGMs), a branch of advanced materials characterized by spatially continuous varying properties. Since its origin in 1984 (see e.g. [9]), this concept has promoted the development of a wide range of functionally graded composite materials (FGCM). These materials are inhomogeneous composites characterized by smooth and continuous variations in both compositional profile and material properties. This feature allows designers to optimize the contribution of each phase of the composite, which has led to an extensive number of applications in many engineering fields. Given the promising capabilities of the employment of carbon nanotubes

---
*Corresponding author.
Email address:* `egarcia28@us.es` (Enrique García-Macías)

as reinforcements in functionally graded materials, it is essential to develop theoretical models to predict the response of full-scale functionally graded carbon nanotube reinforced (FG-CNTRC) structural elements. However, because of its inherent complexity, FG-CNTRC structures are difficult to manufacture according to its exact design specifications. Hence, undesirable process-induced uncertainties may arise. Since the mechanical properties of the constituent materials (matrix/CNTs) may vary statistically, as well as the uncertainties inherent in the fabrication technique, the mass and stiffness matrices of FG-CNTRC structural elements are stochastic in nature. Therefore, the properties of FG-CNTRC materials should be quantified probabilistically. In order to probabilistically assess the behavior of FG-CNTRC structures, randomness must be taken into consideration in three coupled aspects: (i) uncertainty in the material properties, (ii) uncertainty associated with the leap from nano to macroscale through an homogenization framework and (iii) uncertainty in the reinforcement grading profile.

The number of publications on static and dynamic deterministic analysis of CNTRC and FG-CNTRC structural elements has increased considerably in recent years with plenty of newly published results. Linear distributions of single-walled carbon nanotubes (SWCNTs) within an isotropic matrix were proposed by Shen [10]. In this work, it is shown that nonlinear load-bending moment curves of FG-CNTRC plates in thermal environments can be significantly increased as a result of a functionally graded reinforcement. Zhu et al. [11] carried out bending and free vibration analysis of FG-CNTRC plates by FEM based on first-order shear deformation plate theory (FSDT) with similar conclusions. Yas and Heshmati implemented the Timoshenko beam theory to analyze the vibration of straight uniform [12] and linear [13] FG-CNTRC beams subjected to moving loads. Zhang et al. [14] proposed a state-space Levy method for the vibration analysis of FG-CNT composite plates subjected to in-plane loads based on higher-order shear deformation theory. This research analyzed three different symmetric linear distributions of the reinforcements along the thickness, namely UD, FG-X and FG-O. They concluded that FG-X provides the largest frequency and critical buckling in-plane load. On the contrary, the frequency for the FGO-CNT plate was the lowest. Zhang and Liew [15] presented detailed parametric studies of the large deflection behaviors of FG-CNTRC quadrilaterals for different types of CNT distributions. They concluded that the geometric parameters such as side angle, thickness-to-width ratio or plate aspect ratios are more significant than material parameters such as CNT distribution and CNT volume fraction. García-Macías et al. [16] proposed a shell finite element formulation based on the Hu-Washizu principle in general curvilinear coordinates for the simulation of FG-CNTRCs. In particular, it is applied for an exhaustive parametric analysis of the static response and free vibration characteristics of FG-CNTRC skew plates with uniform and linear CNT distributions. It should be noted that all the aforementioned works only took account of linear reinforcement grading profiles.

Uncertainty propagation in nanocomposite structures remains as an unsolved issue. Rouhi and Rohani [17] analyzed the probabilistic response characteristics of a thin-walled nanocomposite cylinder subjected to buckling instability. They employed micromechanical approaches based on the Eshelby-Mori-Tanaka method for the mathematical modeling of randomly distributed carbon nanofibers (CNFs) in a thermoset polymer material. By using a dual metamodeling procedure, uncertainty in CNF material properties, CNF waviness and CNF-matrix interphase were taken into consideration to carry out a reliability-based design optimization in terms of a prescribed maximum probability of failure. Ghasemi et al. [18] proposed a Kriging metamodel-based probabilistic optimization procedure. By linking the different scales (nano-, micro-, meso- and macro- scales) by multi-scale analysis, the Eshelby-Mori-Tanaka model and finite element method, they considered three different uncertainty sources: material uncertainties (length, waviness, agglomeration, orientation and disperson of CNTs), structural uncertainties (geometry, boundary and loading conditions) and modeling uncertainties (discretization and approximation errors). Their results showed that the failure probability strongly depends on the CNT parameters, especially the CNT volume fraction and the waviness. In addition, they also concluded that the influence of the CNT agglomeration is nearly negligible.

The objective of the present study is to investigate the effects of the randomness in CNT distribution coupled with the material uncertainties on the vibrational properties of FG-CNTRC plates. Most researchers restrict the aim of their studies to the analysis of composite materials with uniform or linear grading profiles. However, because of its manufacturing complexity, FG-CNTRC structures may be expected to present process-induced uncertainties that make these linear distributions rather improbable. Thus, two main sources of uncertainty are considered: uncertainty in the material properties (matrix/CNT) and uncertainty in the reinforcement grading profile which, in turn, propagates the prior uncertainties within the thickness of the specimen. To increase the computational efficiency, the expensive-to-evaluate finite element model is surrogated by two metamodels, Kriging and High-Dimensional Model Representations (RS-HDMR). In these two cases, the actual finite element model is replaced by a response surface model, making the process computationally efficient and cost effective. Random samples are drawn uniformly over the entire domain ensuring good prediction capability of the constructed metamodels in the whole design space including the tail regions. The experience in the application of these techniques for the uncertainty analysis of composite materials is extensive and with excellent results. The RS-HDMR approach has been employed in many different fields [19–21]. The uncertainty of the dynamic characteristics of

2

angle-ply composite plates was studied by Sudip et al. [22], as well as the effects of noise on stochastic frequency response functions [23] and thermal uncertainty propagation in laminated composite plates [24]. Sudip et al. [25] also employed the Kriging metamodel to analyze the uncertainty propagation in the free vibration characteristics of laminated shallow doubly curved shells. In this paper, in order to cross-validate the results for constructing the metamodels, a sensitivity analysis is carried out. Furthermore, the efficacy of both metamodels are compared to direct Monte Carlo simulation (MCS) with accurate results and a drastic reduction of computation cost. Motivated by [16], a finite element formulation based on a modified Hu-Washizu potential principle is employed. Four-noded elements with five degrees of freedom at each node are implemented with consideration of transverse shear strains by first-order shear deformation theory (FSDT). The element is consistently formulated by independent approximations of displacements (bilinear), strains and stresses (piecewise constant within subregions). The paper is organized as follows, Section 2: definition of functionally graded carbon nanotube plates; Section 3: finite element formulation; Section 4: Surrogate modeling: Kriging and RS-HDMR metamodels; Section 5: results and discussion; and Section 6: Conclusions.

2. Functionally graded CNTRC plates

In the present paper, FG-CNTRC plates with uniform thickness h, length a and width b are considered as shown in Fig. 1. Also shown are the four most popular linear reinforcement grading profiles in the literature. UD-CNTRC represents the uniform distribution and FG-V, FG-O and FG-X CNTRC are linear functionally graded distributions of carbon nanotubes in the thickness direction of the composite plates. The effective material properties of the two-phase nanocomposites mixture of uniaxially aligned CNTs reinforcements and a polymeric matrix, can be estimated according to the Mori-Tanaka scheme [26] or the rule of mixtures [3, 27]. The accuracy of the extended rule of mixtures (EROM) has been widely discussed and a remarkable synergism with the Mori-Tanaka scheme for functionally graded ceramic-metal beams is reported in [28]. For simplicity and convenience, in the present study, the extended rule of mixture was employed by introducing the CNT efficiency parameters and the effective material properties of CNTRC plates can thus be written as [10]
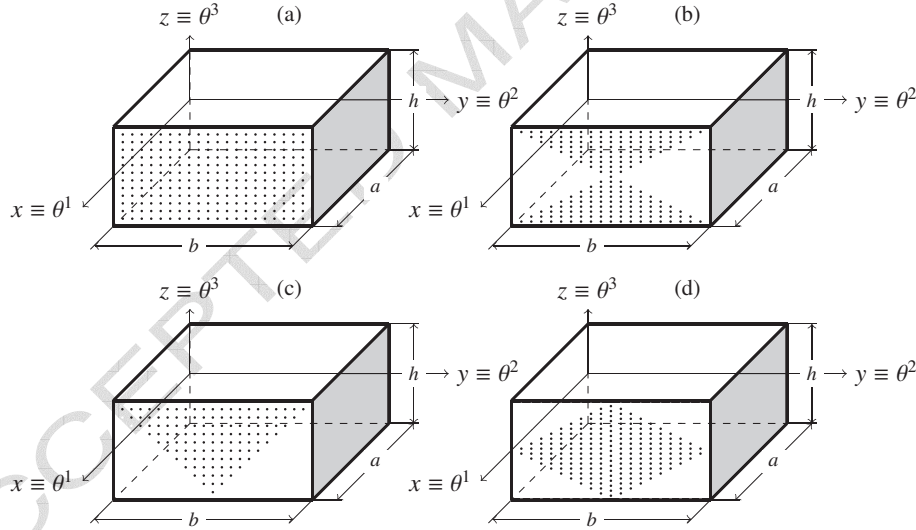
Figure 1: Geometry and linear configurations of the functionally graded carbon nanotube-reinforced (FG-CNTRC) plates. (a) UD CNTRC plate; (b) FG-V CNTRC plate; (c) FG-O CNTRC plate; (d) FG-X CNTRC plate.

$$E_{11} = \eta_1 V_{CNT} E_{11}^{CNT} + V_m E^m \tag{1a}$$

$$\frac{\eta_2}{E_{22}} = \frac{V_{CNT}}{E_{22}^{CNT}} + \frac{V_m}{E^m} \tag{1b}$$

$$\frac{\eta_3}{G_{12}} = \frac{V_{CNT}}{G_{12}^{CNT}} + \frac{V_m}{G^m} \tag{1c}$$

where E_{11}^{CNT}, E_{22}^{CNT} and G_{12}^{CNT} indicate the Young's moduli and shear modulus of SWCNTs, respectively, and E^m and G^m represent the corresponding properties of the isotropic matrix. To account for the scale-dependent material

3

properties, the CNT efficiency parameters, η_j (j=1,2,3), were introduced and can be calculated by matching the effective properties of the CNTRC obtained from a molecular dynamics (MD) or multi-scale simulation with those from the rule of mixtures. V_{CNT} and V_m are the volume fractions of the carbon nanotubes and matrix, respectively, and the sum of the volume fractions of the two constituents should equal unity. Similarly, the thermal expansion coefficients, α_{11} and α_{22}, in the longitudinal and transverse directions respectively, Poisson's ratio ν_{12} and the density ρ of the nanocomposite plates can be determined in the same way as

$$\nu_{12} = V_{CNT}\nu_{12}^{CNT} + V_m\nu^m \tag{2a}$$

$$\rho = V_{CNT}\rho^{CNT} + V_m\rho^m \tag{2b}$$

$$\alpha_{11} = V_{CNT}\alpha_{11}^{CNT} + V_m\alpha^m \tag{2c}$$

$$\alpha_{22} = (1 + \nu_{12}^{CNT})V_{CNT}\alpha_{22}^{CNT} + (1 + \nu^m)V_m\alpha^m - \nu_{12}\alpha_{11} \tag{2d}$$

where ν_{12}^{CNT} and ν^m are Poisson's ratios, and α_{11}^{CNT}, α_{22}^{CNT} and α^m are the thermal expansion coefficients of the CNT and matrix, respectively. Note that ν_{12} is considered to be constant over the thickness of the functionally graded CNTRC plates. The other effective mechanical properties are defined as follows

$$\begin{aligned} E_{33} &= E_{22}, & G_{13} &= G_{12}, & G_{23} &= \tfrac{1}{2}\tfrac{E_{22}}{1+\nu_{23}}, \\ \nu_{13} &= \nu_{12}, & \nu_{31} &= \nu_{21}, & \nu_{32} &= \nu_{23} = \nu_{21}, \\ \nu_{21} &= \nu_{12}\tfrac{E_{22}}{E_{11}} \end{aligned} \tag{3}$$

The uniform and three types of linear functionally graded distributions of the carbon nanotubes along the thickness direction of the nanocomposite plates shown in Fig. 1 are assumed to be

$$V_{CNT} = V_{CNT}^* \qquad \text{(UD \quad CNTRC)}$$

$$V_{CNT} = \frac{4|z|}{h}V_{CNT}^* \qquad \text{(FG-X \quad CNTRC)}$$

$$V_{CNT} = (1 + \frac{2z}{h})V_{CNT}^* \qquad \text{(FG-V \quad CNTRC)} \tag{4}$$

$$V_{CNT} = 2(1 - \frac{2|z|}{h})V_{CNT}^* \quad \text{(FG-O \quad CNTRC)}$$

In the present work, the source of uncertainty in the reinforcement grading profile is considered as a variation from the linear distribution. In order to take into account this effect, a general distribution shape function $f(z)$ can be implemented. For a given volume fraction of inclusions V_{CNT}^*, the distribution of CNTs as a function of the z coordinate can be derived as

$$V_{CNT}(z) = V_{CNT}^* \cdot \frac{f(z) \cdot h}{\int_{-h/2}^{h/2} f(z)\,\mathrm{d}z} \tag{5}$$

Different expressions for this distribution shape function can be assumed. Some of the most employed distributions in the literature are power-law functions (P-FGM), exponential functions (E-FGM) and sigmoid functions (S-FGM) [29]. In the present paper, P-FGM is selected. For instance, in the case of FG-V and FG-X distributions, the CNT volume fraction defined by P-FGM, P-FGV and P-FGX respectively, adopts the following expressions

$$\begin{aligned} f(z) &= (\tfrac{h-2z}{2h})^k & \text{(P-FGV)} \\ f(z) &= \begin{cases} \left(\tfrac{2}{h}z\right)^k & 0 \le z \le \tfrac{h}{2} \\ \left(-\tfrac{2}{h}z\right)^k & -\tfrac{h}{2} \le z \le 0 \end{cases} & \text{(P-FGX)} \end{aligned} \tag{6}$$

where the variation around the linear case ($k = 1$) is controlled by the power-law index k. Fig. 2 shows the different profiles obtained by P-FGV and P-FGX for different values of the power law index

3. Finite element formulation

Consider CNTRC plate of length a, width b and thickness t as shown in Fig. 1. In this section, the more general theoretical formulation developed in [16] is adopted here for the case of flat rectangular shells. Denoting by $\mathcal{U}(\gamma)$ the strain energy and by γ and σ the vectors containing the strain and stress components, respectively, a modified potential of Hu-Washizu assumes the form [30]
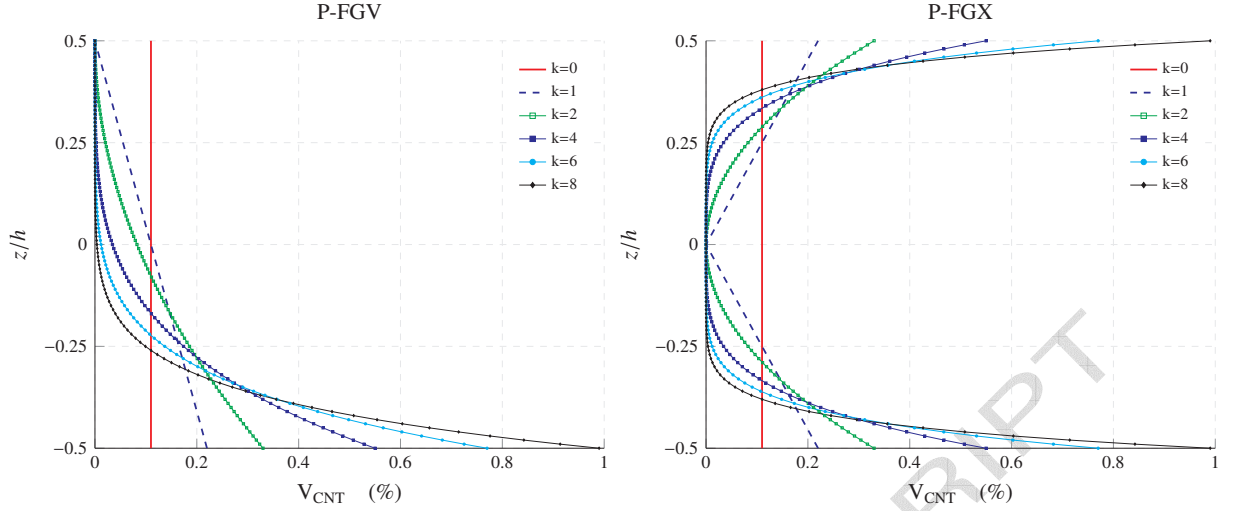
4

P-FGV

P-FGX

Figure 2: Variation of the CNT volume fraction through the thickness defined by the power-law distribution function for different power law indices k, based on FG-V and FG-X linear distributions, namely P-FGV and P-FGX ($V_{CNT}^* = 0.11$).

$$\Pi_{HW}[\mathbf{v}, \gamma, \sigma] = \int_V [\mathcal{U}(\gamma) - \sigma^T (\gamma - \mathbf{D}\,\mathbf{v}) - \Pi_b]\,dV - \int_{S_{\hat{v}}} (\mathbf{v} - \hat{\mathbf{v}})\,\sigma\,\mathbf{n}\,dS - \int_{S_t} \Pi_t\,dS \tag{7}$$

In Eq. (7), $\mathbf{v}$ and the index b represent the displacement vector and the body forces, respectively, whereas $\hat{\mathbf{v}}$ are prescribed displacements on the part of the boundary in which displacements are prescribed ($S_{\hat{v}}$).

The displacement field is constructed by first-order shear deformation. Hence the in-plane deformation $\gamma_{\alpha\beta}$ is expressed in terms of the extensional ($_0\gamma_{\alpha\beta}$) and flexural ($_1\gamma_{\alpha\beta}$) components of the Cauchy-Green strain tensor as

$$\gamma_{\alpha\beta} = {_0\gamma_{\alpha\beta}} + \theta^3\,{_1\gamma_{\alpha\beta}}. \tag{8}$$

The constitutive equations are written in Voigt's notation in the form

$$\begin{bmatrix} s_{11} \\ s_{22} \\ s_{12} \\ s_{23} \\ s_{13} \end{bmatrix} = \begin{bmatrix} Q_{11}(z) & Q_{12}(z) & 0 & 0 & 0 \\ Q_{12}(z) & Q_{22}(z) & 0 & 0 & 0 \\ 0 & 0 & Q_{66}(z) & 0 & 0 \\ 0 & 0 & 0 & Q_{44}(z) & 0 \\ 0 & 0 & 0 & 0 & Q_{55}(z) \end{bmatrix} \cdot \begin{bmatrix} \gamma_{11} \\ \gamma_{22} \\ \gamma_{12} \\ \gamma_{23} \\ \gamma_{13} \end{bmatrix} \tag{9}$$

$$\begin{aligned} Q_{11} &= \frac{E_{11}}{1 - \nu_{12}\cdot\nu_{21}}, \quad Q_{22} = \frac{E_{22}}{1 - \nu_{12}\cdot\nu_{21}}, \quad Q_{12} = \frac{\nu_{21}\cdot E_{11}}{1 - \nu_{12}\cdot\nu_{21}}, \\ Q_{66} &= G_{12}, \qquad\qquad Q_{44} = G_{23}, \qquad\qquad Q_{55} = G_{13} \end{aligned} \tag{10}$$

Note that Q_{ij} varies with z according to the grading profile of the CNTRC along the thickness. Thus, the components of the extensional stiffness C_E, bending extensional coupling stiffness C_C, bending stiffness C_B, and transverse shear stiffness C_S are defined by the following integrals

$$\begin{aligned} (C_E^{ij}, C_C^{ij}, C_B^{ij}) &= \int_{-h/2}^{h/2} Q_{ij}(z) \cdot (1, z, z^2)\,dz \quad (i, j = 1, 2, 6), \\ C_S^{ij} &= \frac{1}{ks} \int_{-h/2}^{h/2} Q_{ij}(z)\,dz \quad (i, j = 4, 5) \end{aligned} \tag{11}$$

where ks denotes the transverse shear correction factor for FGM, given by [31]

$$ks = \frac{6 - (\nu_i V_i + \nu_m V_m)}{5} \tag{12}$$

From Eq. (8) and the thin body assumption, the strain-energy density per unit of area at the reference surface can be expressed as

$$U = \int_{-h/2}^{h/2} \Phi\,dz = \int_{-h/2}^{h/2} \left[\frac{1}{2}\,C^{\alpha\beta\gamma\delta} \left({_0\gamma_{\alpha\beta}} + \theta^3\,{_1\gamma_{\alpha\beta}} \right) \left({_0\gamma_{\gamma\delta}} + \theta^3\,{_1\gamma_{\gamma\delta}} \right) + 2\,E^{\alpha3\beta3}\,\gamma_{\alpha3}\,\gamma_{\beta3} \right] dz \tag{13}$$

5

Expression (13) for the strain energy can be represented as the sum of the extensional (U_E), bending (U_B), coupling (U_C) and transverse shear (U_S) strain energy as

$$U_{Total} = U_E + U_B + U_C + U_S =$$
$$= \frac{1}{2} \left({}_0\gamma^T \, \mathbf{C_E} \, {}_0\gamma + {}_1\gamma^T \, \mathbf{C_B} \, {}_1\gamma + {}_0\gamma^T \, \mathbf{C_C} \, {}_1\gamma + {}_1\gamma^T \, \mathbf{C_C} \, {}_0\gamma + \gamma_S^T \, \mathbf{C_S} \, \gamma_S \right) \tag{14}$$

The shell element derived in the present study is a four-noded rectangular isoparametric finite element with five degrees of freedom at each node: three components of the displacements u_1, u_2, u_3 and two components of the rotations φ_1, φ_2. Bilinear shape functions N_k are chosen for the components of the displacements and rotations.

The numerical integration over the isoparametric rectangular elements is carried out by a piecewise constant approximation of the linear variation of the strains and stresses. These piecewise constant approximations can be improved by introducing four subdomains over the finite element (see Fig. 3). For example, Fig. 4 illustrates the piecewise approximation of γ_{11} and γ_{22} over two subdomains. In the case of the membrane shear strain γ_{12}, it is approximated by a constant.
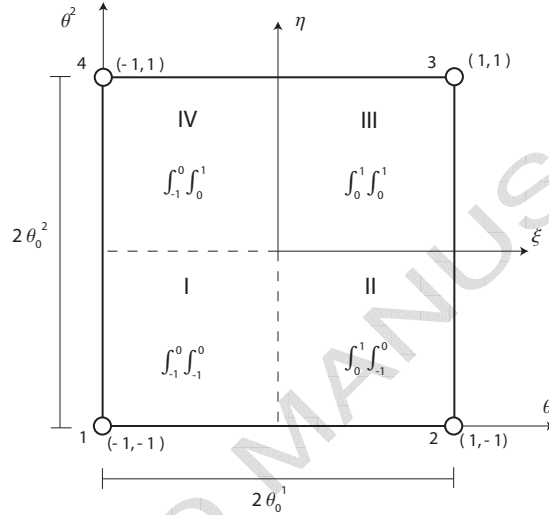

Figure 3: Subdomain areas throughout the isoparametric rectangular finite element.

Considering the piecewise approximations through the four subdomains, the extensional (ε), bending ($kappa$) and shear strain (γ) over every subdomain are defined as

– *Extensional strains* ($\varepsilon_{11}, \varepsilon_{22}, \varepsilon_{12}$) and *Bending strains* ($\kappa_{11}, \kappa_{22}, \kappa_{12}$)

$$(\varepsilon_{11}, \kappa_{11}) = \begin{cases} \left(\varepsilon_{11}^A, \kappa_{11}^A\right) & \text{in} \quad A_I + A_{II} \\ \left(\varepsilon_{11}^B, \kappa_{11}^B\right) & \text{in} \quad A_{III} + A_{IV} \end{cases} \quad , \quad (\varepsilon_{22}, \kappa_{22}) = \begin{cases} \left(\varepsilon_{22}^C, \kappa_{22}^C\right) & \text{in} \quad A_I + A_{IV} \\ \left(\varepsilon_{22}^D, \kappa_{22}^D\right) & \text{in} \quad A_{II} + A_{III} \end{cases} \quad ,$$

$$(\varepsilon_{12}, \kappa_{12}) = (\bar{\varepsilon}_{12}, \bar{\kappa}_{12}) \quad \text{in} \quad A$$

– *Shear strains* (γ_{13}, γ_{23})

$$\gamma_1 = \begin{cases} \gamma_1^A & \text{in} \quad A_I + A_{II} \\ \gamma_1^B & \text{in} \quad A_{III} + A_{IV} \end{cases} \quad , \quad \gamma_2 = \begin{cases} \gamma_2^C & \text{in} \quad A_I + A_{IV} \\ \gamma_2^D & \text{in} \quad A_{II} + A_{III} \end{cases} \tag{15}$$

As a consequence of this approximation, the strain energy term in the Hu-Washizu variational principle takes the form of

$$\int_A U \, dA = \frac{1}{2} \bar{\varepsilon}^T \, \bar{\mathbf{D}}_{\mathbf{E}} \, \bar{\varepsilon} + \frac{1}{2} \bar{\kappa}^T \, \bar{\mathbf{D}}_{\mathbf{B}} \, \bar{\kappa} + \frac{1}{2} \bar{\varepsilon}^T \, \bar{\mathbf{D}}_{\mathbf{C}} \, \bar{\kappa} + \frac{1}{2} \bar{\kappa}^T \, \bar{\mathbf{D}}_{\mathbf{C}} \, \bar{\varepsilon} + \frac{1}{2} \bar{\gamma}^T \, \bar{\mathbf{D}}_{\mathbf{S}} \, \bar{\gamma} \tag{16}$$

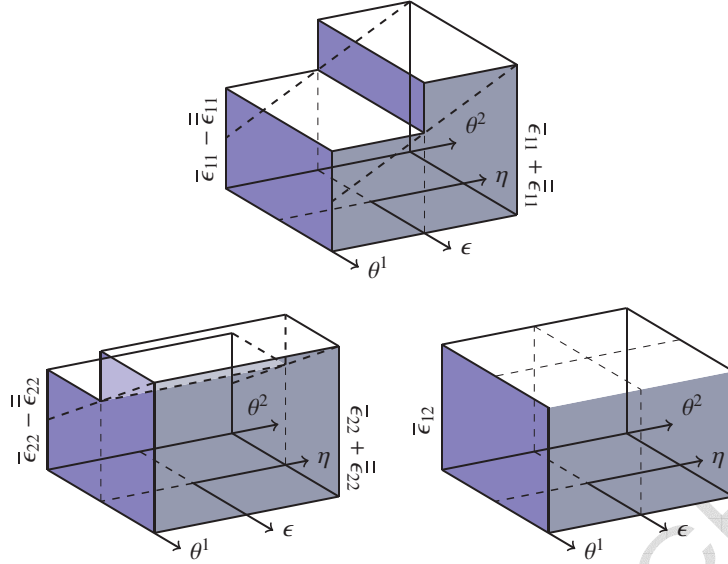where the vectors $\bar{\varepsilon}, \bar{\kappa}$ and $\bar{\gamma}$ are defined by

6

Figure 4: Schematic representation of the piecewise constant extensional strain (ε) approximation.

$$\bar{\varepsilon} = \left\{ \begin{array}{c} \varepsilon_{11}^A \\ \varepsilon_{11}^B \\ \varepsilon_{22}^C \\ \varepsilon_{22}^D \\ 2\,\varepsilon_{12} \end{array} \right\} \quad , \quad \bar{\kappa} = \left\{ \begin{array}{c} \kappa_{11}^A \\ \kappa_{11}^B \\ \kappa_{22}^C \\ \kappa_{22}^D \\ 2\,\kappa_{12} \end{array} \right\} \quad , \quad \bar{\gamma} = \left\{ \begin{array}{c} \gamma_1^A \\ \gamma_1^B \\ \gamma_2^C \\ \gamma_2^D \end{array} \right\} \tag{17}$$

The matrices $\bar{\mathbf{D}}_{\mathbf{E}}$, $\bar{\mathbf{D}}_{\mathbf{B}}$, $\bar{\mathbf{D}}_{\mathbf{C}}$ and $\bar{\mathbf{D}}_{\mathbf{S}}$ are the discretized elasticity matrices according to the four subdomains. In addition, by introducing the matrices

$$\mathbf{A_N} = \mathbf{A_M} = diag\,\{A_I + A_{II}, A_{III} + A_{IV}, A_I + A_{IV}, A_{II} + A_{III}, A\}\,, \tag{18a}$$

$$\mathbf{A_Q} = diag\,\{A_I + A_{II}, A_{III} + A_{IV}, A_I + A_{IV}, A_{II} + A_{III}\} \tag{18b}$$

along with the discretized strain-displacement relationships, the bilinear approximations for the displacements and rotations, and also the discrete parameters for the strains and stresses, the discrete form of the generalized variational principle of Hu-Washizu is given by

$$\begin{aligned} \Pi_{HW} = {} & \frac{1}{2}\,\bar{\varepsilon}^T\,\bar{\mathbf{D}}_{\mathbf{E}}\,\bar{\varepsilon} + \frac{1}{2}\,\bar{\kappa}^T\,\bar{\mathbf{D}}_{\mathbf{B}}\,\bar{\kappa} + \frac{1}{2}\,\bar{\varepsilon}^T\,\bar{\mathbf{D}}_{\mathbf{C}}\,\bar{\kappa} + \frac{1}{2}\,\bar{\kappa}^T\,\bar{\mathbf{D}}_{\mathbf{C}}\,\bar{\varepsilon} + \frac{1}{2}\,\bar{\gamma}^T\,\bar{\mathbf{D}}_{\mathbf{S}}\,\bar{\gamma} \\ & - \frac{1}{2}\left(\mathbf{N}^T\,\mathbf{A_N}\,\bar{\varepsilon} + \bar{\varepsilon}^T\,\mathbf{A_N}\,\mathbf{N}\right) - \frac{1}{2}\left(\mathbf{M}^T\,\mathbf{A_M}\,\bar{\kappa} + \bar{\kappa}^T\,\mathbf{A_M}\,\mathbf{M}\right) - \frac{1}{2}\left(\mathbf{Q}^T\,\mathbf{A_Q}\,\bar{\gamma} + \bar{\gamma}^T\,\mathbf{A_Q}\,\mathbf{Q}\right) \\ & + \frac{1}{2}\left(\mathbf{N}^T\,\mathbf{E}\,\mathbf{\Delta} + \mathbf{\Delta}^T\,\mathbf{E}\,\mathbf{N}\right) + \frac{1}{2}\left(\mathbf{M}^T\,\mathbf{B}\,\mathbf{\Delta} + \mathbf{\Delta}^T\,\mathbf{B}\,\mathbf{M}\right) + \frac{1}{2}\left(\mathbf{Q}^T\,\mathbf{G}\,\mathbf{\Delta} + \mathbf{\Delta}^T\,\mathbf{G}\,\mathbf{Q}\right) \end{aligned} \tag{19}$$

with $\mathbf{N}$, $\mathbf{M}$ and $\mathbf{Q}$ the discretized stress resultants similarly to Eqs. (17). The Hu-Washizu variational principle establishes that if the variation is taken with respect to nodal displacements and rotations ($\mathbf{\Delta}$), strains, and stresses, then all field equations of elasticity and all boundary conditions appear as Euler-Lagrange equations. In particular, the stationary condition for the functional ($\delta\Pi_{HW} = 0$) enforces, after some algebraic manipulation, the discrete equilibrium in terms of nodal displacements and rotations as

$$\left[\mathbf{K}_{Extension} + \mathbf{K}_{Bending} + \mathbf{K}_{Coupling} + \mathbf{K}_{Shear}\right]\,\mathbf{\Delta} = \mathbf{p} \tag{20}$$

Therefore, the stiffness matrix, $\mathbf{K}_{20\times20}$, is defined by the sum of the following four terms

$$\mathbf{K}_{Extension} = \mathbf{A}_N^{-1} \, \bar{\mathbf{D}}_{\mathbf{E}} \, \mathbf{A}_N^{-1} \, \mathbf{E} \,, \tag{21}$$

$$\mathbf{K}_{Bending} = \mathbf{B}^T \, \mathbf{A}_M^{-1} \, \bar{\mathbf{D}}_{\mathbf{F}} \, \mathbf{A}_M^{-1} \, \mathbf{B} \,, \tag{22}$$

$$\mathbf{K}_{Coupling} = \mathbf{B}^T \, \mathbf{A}_M^{-1} \, \bar{\mathbf{D}}_{\mathbf{C}} \, \mathbf{A}_N^{-1} \, \mathbf{E} + \mathbf{E}^T \, \mathbf{A}_N^{-1} \, \bar{\mathbf{D}}_{\mathbf{C}} \, \mathbf{A}_M^{-1} \, \mathbf{B} \,, \tag{23}$$

$$\mathbf{K}_{Shear} = \mathbf{G}^T \, \mathbf{A}_Q^{-1} \, \bar{\mathbf{D}}_{\mathbf{S}} \, \mathbf{A}_Q^{-1} \, \mathbf{G} \,. \tag{24}$$

The eigenvalue problem for the undamped free vibration problem takes the well-known form

$$\mathbf{K}\,\mathbf{u} = \omega^2 \, \mathbf{M}\,\mathbf{u} \,, \tag{25}$$

where $\mathbf{K}$ is the stiffness matrix of the system, $\mathbf{u}$ represents the eigenvectors, ω is the natural frequency in rad/s and $\mathbf{M}$ is the mass matrix of the structure. The consistent element mass matrix is derived by discretizing the kinetic energy

$$\delta \mathcal{U}_K = \frac{1}{2} \int_V \rho \, 2\, \mathbf{v} \, \delta \ddot{\mathbf{v}} dV \,, \tag{26}$$

and by employing the displacement field defined by first-order shear deformation, the consistent mass matrix can be represented by

$$\mathbf{M} = \begin{bmatrix} \mathbf{M}_{11} & \mathbf{M}_{12} & \mathbf{M}_{13} & \mathbf{M}_{14} \\ & \mathbf{M}_{22} & \mathbf{M}_{23} & \mathbf{M}_{24} \\ & & \mathbf{M}_{33} & \mathbf{M}_{34} \\ sym & & & \mathbf{M}_{44} \end{bmatrix}_{20 \times 20} \tag{27}$$

Every $\mathbf{M}_{ij}$ term of the mass matrix, where i and j represent the row and the column respectively, assumes the following form

$$\mathbf{M}_{ij} = \begin{bmatrix} \int_A I_1 \, N_i \, N_j \, dA & \int_A - I_1 \, N_i \, N_j \, dA & 0 & \int_A I_2 \, N_i \, N_j \, dA & \int_A - I_2 \, N_i \, N_j \, dA \\ & \int_A I_1 \, N_i \, N_j \, dA & 0 & \int_A - I_2 \, N_i \, N_j \, dA & \int_A I_2 \, N_i \, N_j \, dA \\ & & \int_A I_1 \, N_i \, N_j \, dA & 0 & 0 \\ & & & \int_A I_3 \, N_i \, N_j \, dA & \int_A - I_3 \, N_i \, N_j \, dA \\ sym & & & & \int_A I_3 \, N_i \, N_j \, dA \end{bmatrix}_{5 \times 5} \tag{28}$$

where the terms I_1, I_2, I_3 are defined by

$$I_1 = \int_{-h/2}^{h/2} \rho(z) dz, \quad I_2 = \int_{-h/2}^{h/2} \rho(z) \cdot z dz, \quad I_3 = \int_{-h/2}^{h/2} \rho(z) \cdot z^2 dz \tag{29}$$

4. Surrogate modeling

In this section, two metamodels are introduced, Kriging and random sampling high dimensional model representation (RS-HDMR). In general, a surrogate model is an approximation of the Input/Output of a main model. The main purpose of a surrogate model is to fit the outcome obtained by a large model, costly in terms of computation, in a more compact and cost-effective way. There are a set of m observations, so called design sites $X = [x_1, \ldots, x_m]^T$ with $x_i \in \mathbb{R}^n$, and a set of corresponding outputs $Y = [y_1, \ldots, y_m]^T$ with $y_i \in \mathbb{R}^q$.

4.1. Kriging metamodel

The Kriging model, originated in geostatistics [32], is a commonly used method of interpolation (prediction) for spatial data. This model expresses the unknown function of interest $y(x)$ for a n dimensional input $x \subseteq D \subseteq \mathbb{R}^n$, as the sum of a regression model $y_r(x)$ and a stochastic function $\mathcal{F}(x)$ as follows [33]

$$y(x) = y_r(x) + \mathcal{F}(x) \tag{30}$$

the function $\mathcal{F}(x)$ is the realization of a stochastic process with mean zero, variance σ^2 and non-zero covariance, $y_r(x)$ is a known regression function dependent on p regression parameters $\beta = [\beta_1, \ldots, \beta_p]$ and defined functions $f_j : \mathbb{R}^n \to \mathbb{R}$ [34]

$$y_r(\beta, x) = f(x)^T \beta \tag{31}$$

It can be understood that $y_r(x)$ globally approximates the design space, meanwhile $\mathcal{F}(x)$ creates the localized deviations so that the Kriging model interpolates the m-sampled data points. The covariance matrix of $\mathcal{F}(x)$ is

$$Cov\left[\mathcal{F}(x^i)\mathcal{F}(x^j)\right] = \sigma^2 R\left[R(\theta, x^i, x^j)\right] \tag{32}$$

between any two of the *m*-sampled data points x^i and x^j. R is a $m \times m$ symmetric matrix with ones along the diagonal. $R_{ij} = R(\theta, x^i, x^j)$ is the correlation model with parameters $\theta = \left[\theta_1, \ldots, \theta_l\right]$. The user can specify a wide variety of correlation functions [35–37] dependent on θ parameters. For example, in the case of a Gaussian correlation function

$$R(x^i, x^j) = exp\left[-\sum_{k=1}^{l} \theta_k \left|x_k^i - x_k^j\right|^2\right] \tag{33}$$

The relation between the predicted estimates, $\hat{y}(x)$ of the response $y(x)$ at an untried point x is defined by the Kriging predictor as follows

$$\hat{y}(x) = f(x)^T \cdot \beta^* + r(x)^T (Y - F \cdot \beta^*) \tag{34}$$

where Y is a column vector of length m that contains the sample values of the frequency responses and F is the $m \times p$ observability matrix $F_{ij} = f_j(x_i)$. $r(x)$ is a vector with the correlations between the design sites and x:

$$r^T(x) = [R(\theta, x_1, x), \ldots, R(\theta, x_m, x)]^T \tag{35}$$

The regression problem $F \cdot \beta \approx Y$ has the generalized least squares solution

$$\beta^* = (F^T \cdot R^{-1} F)^{-1} \cdot F^T \cdot R^{-1} \cdot Y \tag{36}$$

and the variance estimate

$$\sigma^2 = \frac{1}{m} (Y - F \cdot \beta^*)^T \cdot R^{-1} \cdot (Y - F \cdot \beta^*) \tag{37}$$

The matrix R and therefore β^* and σ^2, depend on θ. The optimal choice of θ^* is defined as the maximum likelihood estimator (e.g. best guesses),i.e. the maximizer of

$$\max_{\theta > 0} . \Gamma(\theta_k) = \frac{1}{2}(m \cdot \ln \sigma^2 + \ln |R|) \tag{38}$$

where $|R|$ is the determinant of R. This optimization process results in a k-dimensional unconstrained non-linear optimization problem. Note that for a given set of design data the matrices β^* and the parameters θ_k are fixed. For every new x we just have to compute the vectors $f(x) \in \mathbb{R}^p$ and $x \in \mathbb{R}^m$ and add two simple products. After obtaining the Kriging surrogate model, it is possible to compute an approximation error to evaluate the accuracy of the predicted results. The mean squared error (MSE) of the predictor is defined by

$$MSE = E\left[(\hat{y}(x) - y(x))^2\right] \tag{39}$$

4.2. Random Sampling HDMR

The random sampling high dimensional model representation (RS-HDMR) method is a set of tools explored by Rabitz et al. [38] in order to express the input-output mapping of a high dimensional model with a large number of input variables and a reduced number of samples [39, 40]. The relationship between the input $X = [x_1, \ldots, x_m]^T$ and output variables $X = [f(x_1), \ldots, f(x_m)]^T$ is expressed as [41, 42]:

$$f(X) = f_0 + \sum_{i=1}^{n} f_i(x_i) + \sum_{1 \le i < j \le n} f_{ij}(x_i, x_j) + \ldots + f_{12\ldots n}(x_1, x_2, \ldots, x_m) \tag{40}$$

here the term f_0 is a constant (zeroth order) that stands for the mean contribution of all the inputs to the outputs. The function $f_i(x_i)$ is a first order term giving the effect of variable x_i acting independently upon the output $f(X)$. The function $f_{ij}(x_i, x_j)$ is a second order term describing the cooperative effects of the x_i and x_j upon the output $f(X)$. The higher order terms reflect the cooperative effects of increasing numbers of input variables acting together to influence the output $f(X)$. The last term, $f_{(12\ldots m)}(x_1, x_2, \ldots, x_m)$, reflects any residual *m*th order

9

correlated contribution of all input variables. In most cases, terms up to second order are enough to provide accurate results [43]. The component functions are determined through and averaging process. Firstly, all the input variables are rescaled in the range [0, 1]. Hence, the output response function is defined in the domain of a unit hypercube $K^m = \{(x_1, x_2, \ldots, x_m), i = 1, , m\}$. The component functions of the RS-HDMR have the following form:

$$f_0 = \int_{K^m} f(x)\, \mathrm{d}x \tag{41a}$$

$$f_i(x_i) = \int_{K^{m-1}} f(x)\, \mathrm{d}x^i - f_0 \tag{41b}$$

$$f_{ij}(x_i, x_j) = \int_{K^{m-2}} f(x)\, \mathrm{d}x^{ij} - f_i(x_i) - f_0 \tag{41c}$$

where $\mathrm{d}x^i$ stands for the product $\mathrm{d}x_1\, \mathrm{d}x_2 \ldots \mathrm{d}x_n$ without $\mathrm{d}x_i$ whereas $\mathrm{d}x^{ij}$ denotes the same product without $\mathrm{d}x_i$ and $\mathrm{d}x_j$. The last term $f_{12\ldots n}(x_1, x_2, \ldots, x_n)$ is evaluated from the difference between $f(x)$ and all the other component functions. The zeroth order term f_0 is calculated by the average value of all $f(X)$. The determination of the higher component functions requires the evaluation of high-dimensional integrals that can be approximately calculated by direct Monte-Carlo integration. However this integration requires high computational cost. Approximations by analytical basis functions, such as orthonormal polynomials, provide accurate results with considerably less sampling effort. Thus the first and second order component functions are expressed as

$$f_i(x_i) \approx \sum_{r=1}^{k} \alpha_r^i \varphi_r(x_i) \tag{42a}$$

$$f_{ij}(x_i, x_j) \approx \sum_{p=1}^{l} \sum_{q=1}^{\hat{l}} \beta_{pq}^{ij} \varphi_p(x_i) \varphi_q(x_j) \tag{42b}$$

where k, l and $\hat{l}$ represent the order of the polynomial expansion, α_r^i and β_{pq}^{ij} are constant coefficients to be determined, and $\varphi_r(x_i)$, $\varphi_p(x_i)$ and $\varphi_q(x_j)$ are the orthonormal basis functions. An orthonormal basis function $\varphi_k(x)$ has the following properties in a domain $[a, b]$

$$\text{Zero mean:} \quad \int_a^b \varphi_k(x)\, \mathrm{d}x = 0, \quad k = 1, 2, \ldots \tag{43a}$$

$$\text{Unit norm:} \quad \int_a^b \varphi_k^2(x)\, \mathrm{d}x = 1, \quad k = 1, 2, \ldots \tag{43b}$$

$$\text{Mutually orthogonal:} \quad \int_a^b \varphi_k(x)\varphi_l(x)\, \mathrm{d}x = 0, \quad k \neq l \ldots \tag{43c}$$

From the above condition, the orthonormal polynomials are constructed in the domain [0, 1] as

$$\begin{aligned}
\varphi_1(x) &= \sqrt{3}\,(2x - 1) \\
\varphi_2(x) &= 6\sqrt{5}\left(x^2 - x + \tfrac{1}{6}\right) \\
\varphi_3(x) &= 20\sqrt{7}\left(x^3 - \tfrac{3}{2}x^2 + \tfrac{3}{5}x - \tfrac{1}{20}\right) \\
&\vdots
\end{aligned} \tag{44}$$

The expansion coefficients α_r^i and β_{pq}^{ij} can be determined by a minimization process and Monte Carlo integration which leads to

$$\alpha_r^i \approx \frac{1}{N} \sum_{s=1}^{N} f\left(x^{(s)}\right) \varphi_r\left(x_i^{(s)}\right) \tag{45a}$$

$$\beta_{pq}^{ij} \approx \frac{1}{N} \sum_{s=1}^{N} f\left(x^{(s)}\right) \varphi_p\left(x_i^{(s)}\right) \varphi_q\left(x_j^{(s)}\right) \tag{45b}$$

10

Note that only a set of random samples N is necessary to determine all the RS-HDMR component functions. The MC integration for calculating the expansion coefficients α and β controls the accuracy of RS-HDMR. Variance reduction methods can be employed to improve the accuracy of the Monte Carlo integration without increasing the sample size N. Two methods, the correlation method [39] and ratio control variate method [44], have been successfully applied in connection with the RS-HDMR. In both cases the determination of the expansion coefficients is an iterative process and requires an analytical reference function which has to be similar to $f(x)$. A truncated RS-HDMR expansion can be used as a reference function by calculating its expansion coefficients with a direct Monte Carlo integration. Since the HDMR component functions are independent, the order of the polynomial approximation can be chosen separately for each component function in order to improve the accuracy of the final surrogate model. Thereupon, Ziehn and Tomlin [45] developed an optimization method based on the least square method, which determines the best polynomial order for each of the component functions. Furthermore, a threshold criterion proposed by Ziehn and Tomlin [46] allows to exclude unimportant component functions from the RS-HDMR expansion. The final equation of RS-HDMR up to second order component functions are expressed as

$$f(X) = f_0 + \sum_{i=1}^{n} \sum_{r=1}^{k} \alpha_r^i \varphi_r(x_i) + \sum_{1 \le i < j \le n} \sum_{p=1}^{l} \sum_{q=1}^{\acute{l}} \beta_{pq}^{ij} \varphi_p(x_i) \varphi_q(x_j) \tag{46}$$

4.3. Stochastic approach using Kriging and RS-HDMR

Two main sources of stochasticity are considered for FG-CNT plates: the material properties of the composite phases such as the elastic modulus and the Poisson's ratio of the isotropic matrix, mass densities of the matrix and the CNTs, longitudinal and transverse elastic modulus of the CNTs and volume fraction of CNTs, as well as variations with respect to the linear distribution of CNTs by a power-law model, defined by the power-law index k. A variation of $\pm 10\%$ of the uniformly distributed input parameters is assumed for the material variables. In the case of randomness in the CNTs distribution, a truncated Gaussian distribution is set up with a mean value of $\bar{k} = 1$ and a standard deviation of $\sigma_k = 0.2$ in the range $0 \le k \le 2$. Fig. 5 shows the envelope of all the possible P-FGV reinforcement grading profiles with $V_{CNT}^* = 0.11$ provided by the truncated Gaussian distribution. The random variables mentioned above are examined in three sequential stages:

(a) Variation of the material parameters ($k = 1$): $\left\{ E_m, \rho_m, V_m, E_{11}^{CNT}, E_{22}^{CNT}, \rho_{CNT}, V_{CNT} \right\}$
(b) Variation of the reinforcement grading profile: $\{k\}$
(c) Combined variation of (a) and (b).

In the present study, the first three natural frequencies are considered as the outputs. The random input variables are scaled randomly in the range 0 to 1, hence, the output response functions are thus defined in the domain of an unit hypercube $K^n = \{(x_1, \ldots, x_n), i = 1, \ldots, n\}$. Fig. 6 shows a general flowchart describing the uncertainty representation and propagation steps. Firstly, an initial sample of the design space is generated by MCS which is afterwards used in the construction of the surrogate models. The quality of these initial sample points governs the accuracy of the metamodels. Therefore, the quasi-random sequence of Sobol [47] is utilized to ensure a good uniform distribution of the sample points. The response surface thus represents the result of the structural analysis encompassing every reasonable combination of all the input variables. From this, thousands of combinations of all design variables can be created (via simulation) and a pseudo-analysis performed for each variable set, by simply adopting the corresponding surface values. Once the metamodels are built, they can be used to obtain a representative sample of the first three stochastic natural frequencies and, finally, statistical analysis of the generated data is carried out. In order to check the accuracy of the two proposed metamodels, full scale MCS is also carried out with the same number of original FE analysis as the sampling size.

In order to quantify the contribution of each uncertainty source in the response, a global sensitivity analysis based on RS-HDMR is employed in this study. The orthogonal relationship between the component functions of the RS-HDMR expression implies that the component functions are independent and their action contributes independently to the overall output response. This fact suggests that each individual component function has a direct statistical correlation with the output. Hence, the sensitivity of each component function can be determined by calculating the total and partial variances. The total variance (D) is computed using MC integration for a set of N samples ($X^{(s)} = \left(x_1^{(s)}, x_2^{(s)}, \ldots, x_n^{(s)} \right)$, $s = 1, 2, \ldots, N$ and is defined by

$$D = \int_{K^n} f^2(X)\, dX - f_o^2 \approx \frac{1}{N} \sum_{s=1}^{N} f^2 \left(X^{(s)} \right) - f_o^2 \tag{47}$$

The partial variances (D_i and D_{ij}) obtained by using the properties of orthonormal polynomials are expressed as follows
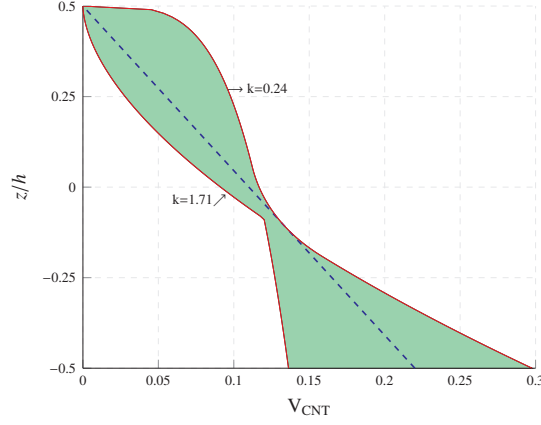
Figure 5: Envelope of all possible grading profiles provided by a FG-V power-law distribution (P-FGV) with $V^*_{CNT} = 0.11$ with different power-law indices (k) according to a truncated Gaussian distribution $\left(\bar{k} = 1, \sigma_k = 0.5 \right)$.

$$D_i = \int_0^1 f_i^2(x_i)\, \mathrm{d}x_i \approx \int_0^1 \left[\sum_{r=1}^k \alpha_r^i \varphi_r(x_i) \right]^2 \mathrm{d}x_i = \sum_{r=1}^k \left(\alpha_r^i \right)^2 \tag{48a}$$

$$D_{ij} = \int_0^1 \int_0^1 f_{ij}^2(x_i, x_j)\, \mathrm{d}x_i\, \mathrm{d}x_j \approx \int_0^1 \int_0^1 \left[\sum_{p=1}^l \sum_{q=1}^{\acute{\imath}} \beta_{pq}^{ij} \varphi_p(x_i) \varphi_q(x_j) \right] = \sum_{p=1}^l \sum_{q=1}^{\acute{\imath}} \left(\beta_{pq} \right)^2 \tag{48b}$$

Finally, the sensitivity indices ($S_{i_1,\dots,i_s}$) are given by

$$S_{i_1,\dots,i_s} = \frac{D_{i_1,\dots,i_s}}{D}, 1 \le i_1 \le i_2 \dots \le i_n \le n \tag{49}$$

so that, $\sum_{i=1}^n S_i + \sum_{1 \le i < j \le n}^n S_{ij} + \dots + S_{1,2,\dots n} = 1$.

The quality of the proposed approximations is appraised by checking the coefficient of determination (R^2). To ensure accuracy, the value of R^2 must be close to one and is expressed as

$$R^2 = \frac{SS_R}{SS_T} = 1 - \frac{SS_E}{SS_T} \quad (0 \le R^2 \le 1) \tag{50}$$

where $SS_T = SS_E + SS_R$ is the total sum of squares, and SS_R and SS_E are the regression sum of squares and the residual sum of squares, respectively. The quality of the surrogate models can also be determined by the Relative Error (RE), computed as

$$RE(\%) = \frac{|F - F'|}{F} \times 100 \tag{51}$$

where F is the actual response and F' is the approximated response using the surrogate models.

5. Results and discussion

In the present study, poly{(m-phenylenevinylene)-co-[(2,5-dioctoxy-p-phenylene)vinylene]} (PmPV) [48] is considered as the matrix and the mean material properties are assumed to be $\nu^m = 0.34$, $\rho^m = 1.15 g/m^3$ and $E^m = 2.1$GPa at room temperature of 300K. The armchair (10,10) SWCNTs are selected as reinforcements with properties taken from the MD simulation carried out by Shen and Zhang [49]. The material properties of these two phases are summarized in Table 1. In this study, it is assumed that the effective material properties are independent of the geometry of the CNTRC plates. The detailed mean material properties of PmPV/CNT for the FG-CNTRC plates are selected from the MD results reported by Han and Elliot [48]. The CNT efficiency parameters η_j can be determined by matching the Young's moduli E_{11} and E_{22} with the counterparts computed by the rule of mixtures. For example, $\eta_1 = 0.149$ and $\eta_2 = 0.934$ for the case of $V^*_{CNT} = 0.11$, and $\eta_1 = 0.150$ and $\eta_2 = 0.941$ for the case of $V^*_{CNT} = 0.14$, and $\eta_1 = 0.149$ and $\eta_2 = 1.381$ for the case of $V^*_{CNT} = 0.17$. In addition, we assume that $\eta_3 = \eta_2$ and $G_{23} = G_{13} = G_{12}$. A fully clamped FG-CNTRC plate is considered having
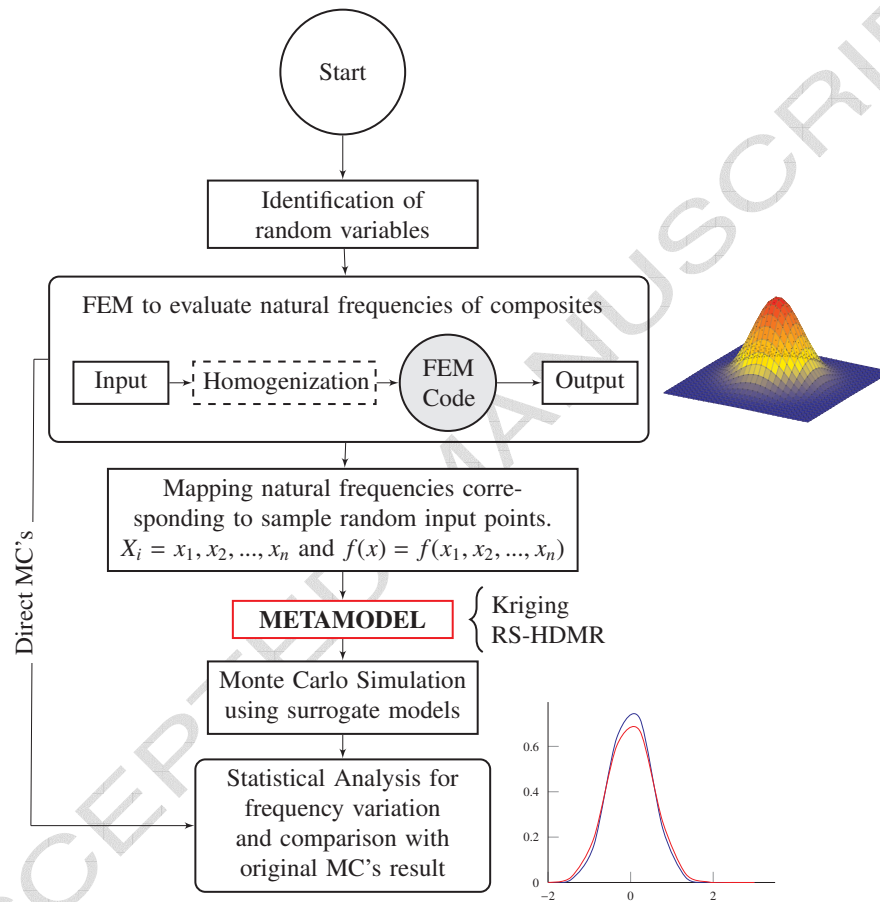
12

Figure 6: Flowchart of stochastic free vibration analysis of FG-CNTRC plates using Kriging and RS-HDMR metamodels.

Table 1: Mean material properties of poly{(m-phenylenevinylene)-co-[(2,5-dioctoxy-p-phenylene)vinylene]} (PmPV)[11] at room temperature of 300K and (10,10) single walled carbon nanotubes (SWCNT)[49].

(10,10) SWCNT [49]	PmPv (T=300K)[11]
$E_{11}^{CNT} = 5.6466$TPa	$E^m = 2.1$GPa
$E_{22}^{CNT} = 7.0800$TPa	$\nu^m = 0.34$
$G_{12}^{CNT} = 1.9445$TPa	
$\nu_{12}^{CNT} = 0.175$	

square plan form $a/b = 1$ and length to thickness ratio $a/h = 10$. According to the general framework presented in section 4.3, and due to paucity of space, only a few important representative results are given. In this section, the nondimensional frequency parameter λ is defined for composites by using the matrix material properties as follows

$$\lambda = \omega \frac{b^2}{\pi^2} \sqrt{\frac{\rho^m h}{D}}; \quad D = E^m h^3 / 12(1 - \nu^{m2}) \tag{52}$$

5.1. Convergence and comparison studies

The present methodology is validated with the results available in the open literature. Fig. 7 presents the error in the determination of the first three non-dimensional natural frequencies for $PmPv/CNT$ FG-CNTRC fully clamped plates (CCCC) with four different linear reinforcement profiles (UD, FG-V, FG-O and FG-X), $V_{CNT}^* = 0.11$, $a/b = 1$ and $a/t = 10$. The error is defined as the relative difference between the results obtained by the proposed method and the ones provided by Zhu et al. [11]. Convergence studies are performed using different uniform mesh divisions of 4×4, 8×8, 12×12, 16×16, 20×20 and 24×24 wherein 12×12 is found to provide accurate results with differences below 5%. This discretization of a 12×12 mesh on the plan area with 144 elements and 169 nodes is used for all the following results. In order to select the initial sample size, another convergence analysis is carried out with respect to R^2 and the maximum error (ME) of the Kriging and RS-HDMR metamodels for different sample sizes as described in Table 2. According to these results, a sample size of 256 is chosen to optimize the computation time for the combined variation of all the input parameters with R^2 around 100%, indicating high accuracy of the fitted models. While evaluating the statistics of responses through full scale direct MCS, the computational time is excessively high because it involves a high number of repeated FE analyses. However, in the present methodology MCS is conducted in conjunction with the two proposed surrogate models which drastically reduces the computational cost. In particular, the required computational time with respect to direct MCS in the present methodology is observed to be around 1/40 and 1/30 for Kriging and RS-HDMR respectively. This provides an efficient and affordable way to computationally simulate the uncertainties in natural frequency. All the statistical analyses are compared to the results provided by direct MCS with 10.000 samples wherein a good agreement is observed in all cases.

5.2. Statistical analysis

The random input variables are scaled randomly in the range 0 to 1. For the material variables, a lower and upper limits of ±10% variation are assumed with respect to the mean values for the uniformly distributed input parameters. In the case of the reinforcement grading profile, a truncated Gaussian distribution (1,0.5) is set up for values of k varying from 0 to 2. Metamodels are formed to generate the first three natural frequencies of CCCC FG-CNTRC plates. In the case of the Kriging metamodels, a second order polynomial regression function and a Gaussian correlation are employed. For the RS-HDMR metamodels, first and second order component functions with orthonormal polynomials up to third order are utilized. Fig. 8 shows the probability density functions obtained by the original MCS with respect to the first natural frequency (λ_1) for simultaneous variation of the material parameters for fully clamped FG-CNTRC plates with four different linear grading profiles (UD, FG-V, FG-O and FG-X). It can be seen that the FG-X plates lead to the stiffest solutions and possess the highest frequency parameters. The explanation of this phenomenon is that reinforcements distributed closer to the extremes result in stiffener plates than those distributed nearer to the mid-plane. Table 3 presents the comparative study between the direct MCs and the surrogate models, Kriging and RS-HDMR, for maximum values, minimum values and percentage of difference for the first three natural frequencies obtained due to combined variability in the material parameters for CCCC FG-CNTRC with the four linear reinforcement distributions. Fig. 9 shows a sample scatter plot describing the relationship between the original FE model and the constructed metamodels for natural frequencies. The low scatter of the points around the diagonal line corroborates that the metamodels are both formed
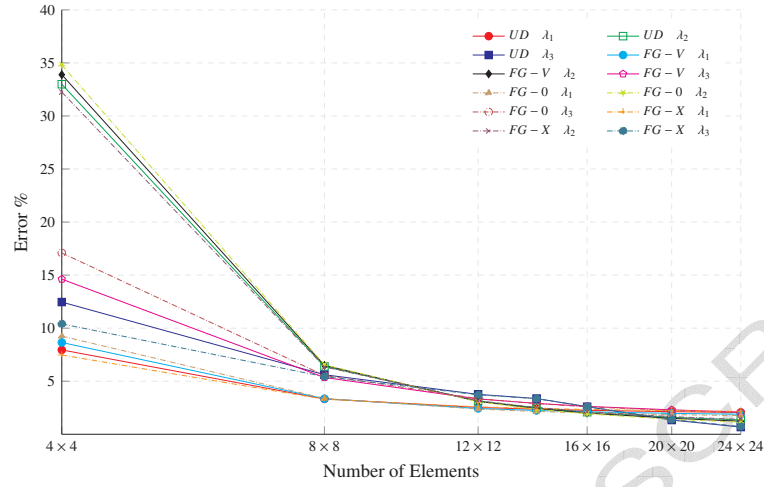
14

Figure 7: Convergence of errors of the first three frequency parameters (λ_i, $i = 1, 2, 3$) with respect to the results provided by Zhu et al. [11] and to the mesh size (N×N) of CCCC FG-CNTRC plates ($a/b = 1$, $h/b = 0.1$ and $\overline{V}^*_{CNT} = 0.11$).

Table 2: Convergence study for the coefficient of determination $\left(R^2\right)$ and maximum error (ME) of the Kriging and RS-HDMR metamodels with different sample sizes of CCCC P-FGV plates ($a/b = 1$, $h/b = 0.1$ and $\overline{V}^*_{CNT} = 0.11$).

| Sample size	Metamodel	Parameter	λ_1	λ_2	λ_3
64	Kriging	R^2	99.998	99.996	99.999
		ME (%)	0.067	0.091	0.059
	RS-HDMR	R^2	98.839	98.688	98.894
		ME (%)	1.141	1.321	1.131
128	Kriging	R^2	99.999	99.997	99.999
		ME (%)	0.058	0.084	0.053
	RS-HDMR	R^2	98.793	98.793	98.810
		ME (%)	1.054	1.103	1.047
256	Kriging	R^2	99.999	99.999	99.999
		ME (%)	0.044	0.040	0.040
	RS-HDMR	R^2	99.918	99.536	99.940
		ME (%)	0.569	0.745	0.511
512	Kriging	R^2	99.999	99.998	99.999
		ME (%)	0.048	0.056	0.038
	RS-HDMR	R^2	99.924	99.546	99.948
		ME (%)	0.529	0.718	0.382
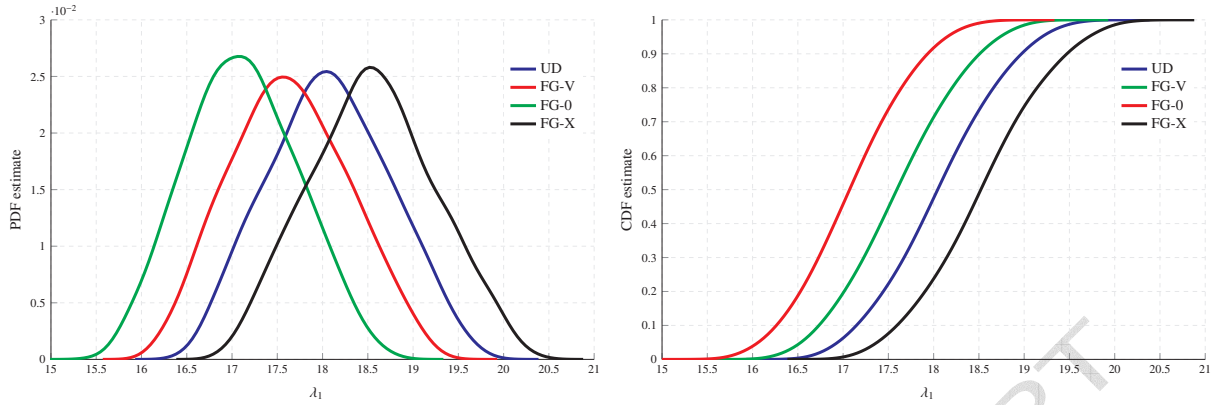
Figure 8: Probability density functions (PDF) and cummulative density functions (CDF) of CCCC FG-CNTRC plates with linear grading profiles and simultaneous variation of the material parameters. ($a/b = 1$, $h/b = 0.1$ and $\overline{V}^{*}_{CNT} = 0.11$, 10.000 samples).

with accuracy. Due to space limitations, in all the subsequent analyses, only results of the uncertainty of the FG-V distribution (P-FGV) will be presented. Fig. 10 shows the comparison of the probability density functions (PDF) obtained by direct MCS and the two surrogate models for the three cases of uncertainty presented in section 4.3. All the plots obtained by both metamodels are checked and found to be in good agreement ensuring efficiency and accuracy. Global sensitivity analysis using RS-HDMR is performed for significant input parameter screening. The sensitivity indices for each input parameter (including the interaction effects) corresponding to different output responses are shown in Fig. 11, while a typical interaction surface between k and E_{11}^{CNT} corresponding to the second order component function of the fundamental frequency is given in Fig. 12. It is observed that the matrix parameters have a predominant effect on sensitivity. A significant effect of the power-law index k is found on the first and third natural frequencies with considerable contribution from the volume fraction of inclusions V_{CNT}^{*}. It is also noticeable the null sensitivity due to random variation of the transverse elastic modulus of CNTs, E_{22}^{CNT}. Table 4 represents the minimum values, maximum values, mean values and standard deviation using the two proposed metamodels for the first three natural frequencies obtained due to individual variability of all the variables.

Finally, some new physical insights are drawn on the dynamic behavior of P-FGV plates by studying the transient response in the frequency domain and a comparison of the stochastic and deterministic mode shapes. The transient response of a CCCC P-FGV plate under impulse loading is considered to ascertain the corresponding amplitude (in dB) of the frequency response function (FRF) as represented in Fig. 13. The Effective Independence method (EFI) [50] was employed to select the optimal positions of three points, two response points (P-1 and P-2) and one driving point (DP). This methodology is based on the maximization of the determinant of the Fisher information matrix (FIM), defined as the product of the mode shape matrix and its transpose. The principal idea of this method is based on the linear independence of the mode shapes. Proportional Rayleigh damping is assumed by imposing damping ratios of 1% for the first two natural modes. Higher frequency shows wider volatility in the simulation bounds of FRF compared to the lower frequency ranges. It is noticeable that the isolated randomness in the power-law index (k) does not lead to great differences in the FRFs. Nevertheless, its simultaneous variation along with the material parameters enlarges the shifts around the resonance peaks and widens the FRF bounds. This can be attributed to the propagating effect of k, which not only incorporates variation by itself, but also scatters the randomness of the rest of the variables, set up at mid-plane level, along the thickness of the plates. Fig. 14 shows the comparison between the deterministic modes and the mean of the stochastic modes through the assessment of the MAC (Modal Assurance Criterion) matrix. In the case of the uncertainty in the material parameters (a), the mode shapes do not change substantially with zero values along the diagonal of the matrix. On the contrary, the incorporation of the uncertainty in the power-law index (k) does change the characteristics of some mode shapes. This effect, which remains in stage (c) with simultaneous variation of all the input parameters, highlights the propagating effect of k along the thickness of the plates.
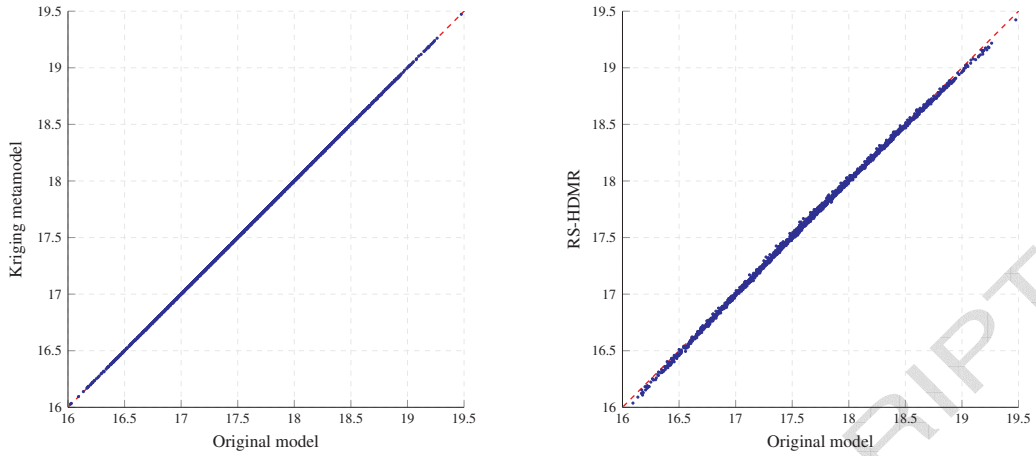
Figure 9: Scatter plot of Kriging and RS-HDMR metamodels with respect to the original model for the first natural frequency (λ_1) for simultaneous variation of the material parameters (CCCC UD-CNTRC plate, $a/b = 1$, $h/b = 0.1$, $\overline{V}_{CNT} = 0.11$).

Table 3: Comparative study between MCS (10.000 samples) and Kriging and RS-HDMR (256 samples) for maximum values, minimum values and percentage of difference for first three frequency parameters for CCCC FG-CNTRC square plates. ($a/b = 1$, $h/b = 0.1$ and $\overline{V}^*_{CNT} = 0.11$).

PF	Parameter	λ_1: First natural frequency				λ_2: Second natural frequency				λ_3: Third natural frequency			
		MC	Kriging	RS-HDMR	Diff. (%)	MC	Kriging	RS-HDMR	Diff. (%)	MC	Kriging	RS-HDMR	Diff. (%)
UD	Max. Val.	19.94	20.03	19.89	-0.46 \ 0.23	26.20	26.27	26.15	-0.30 \ 0.18	38.44	38.60	38.36	-0.41 \ 0.22
	Min. Val.	16.38	16.44	16.59	-0.36 \ -1.26	21.52	21.64	21.80	-0.56 \ -1.32	31.58	31.73	31.99	-0.45 \ -1.28
	Mean. Val.	18.08	18.08	18.07	-0.01 \ 0.01	23.77	23.78	23.77	-0.01 \ 0.01	34.87	34.87	34.87	-0.01 \ 0.01
	Standard deviation	0.66	0.66	0.66	0.37 \ 0.08	0.90	0.89	0.89	0.49 \ 0.13	1.29	1.29	1.29	0.41 \ 0.09
FG-V	Max. Val.	19.48	19.42	19.28	0.28 \ 1.03	25.96	25.90	25.72	0.24 \ 0.93	37.74	37.62	37.36	0.30 \ 0.99
	Min. Val.	16.02	15.96	16.18	0.41 \ -0.98	21.37	21.29	21.64	0.37 \ -1.27	31.08	30.93	31.39	0.50 \ -1.01
	Mean. Val.	17.63	17.63	17.66	0.03 \ -0.16	23.53	23.52	23.57	0.03 \ -0.15	34.18	34.17	34.23	0.03 \ -0.15
	Standard deviation	0.65	0.64	0.65	1.66 \ -0.16	0.89	0.88	0.89	1.70 \ -0.13	1.27	1.25	1.27	1.68 \ -0.16
FG-O	Max. Val.	18.88	18.90	18.60	-0.07 \ 1.50	25.26	25.26	24.97	-0.03 \ 1.14	36.91	36.94	36.44	-0.08 \ 1.29
	Min. Val.	15.37	15.46	15.45	-0.57 \ -0.51	20.69	20.81	20.81	-0.62 \ -0.62	30.11	30.29	30.28	-0.59 \ -0.57
	Mean. Val.	17.11	17.10	17.10	0.07 \ 0.03	22.95	22.93	22.94	0.07 \ 0.03	33.48	33.46	33.47	0.07 \ 0.03
	Standard deviation	0.61	0.61	0.61	0.86 \ -0.12	0.85	0.84	0.85	0.68 \ -0.07	1.22	1.21	1.22	0.77 \ -0.10
FG-X	Max. Val.	20.43	20.49	20.16	-0.30 \ 1.31	26.82	26.97	26.46	-0.54 \ 1.34	39.21	39.34	38.70	-0.32 \ 1.31
	Min. Val.	16.83	16.78	17.10	0.33 \ -1.57	22.04	22.01	22.42	0.12 \ -1.75	32.33	32.22	32.82	0.35 \ -1.49
	Mean. Val.	18.55	18.55	18.56	0.00 \ -0.03	24.36	24.36	24.36	0.00 \ -0.03	35.62	35.62	35.63	0.00 \ -0.03
	Standard deviation	0.68	0.69	0.69	-0.82 \ -1.08	0.92	0.92	0.93	-0.83 \ -1.03	1.32	1.33	1.33	-0.83 \ -1.07

Table 4: Uncertainty analysis due to individual variability of all the input variables by a Kriging and RS-HDMR meatamodels (256 samples) for the first three natural frequencies for CCCC P-FGV plates. ($a/b = 1$, $h/b = 0.1$ and $\overline{V}^*_{CNT} = 0.11$).

| Metamodel	Value	ρ_{CNT}			ρ_m			E_m			E_{11}^{CNT}			E_{22}^{CNT}			V_{CNT}^*			k		
		λ_1	λ_2	λ_3	λ_1	λ_2	λ_3	λ_1	λ_2	λ_3	λ_1	λ_2	λ_3	λ_1	λ_2	λ_3	λ_1	λ_2	λ_3	λ_1	λ_2	λ_3
KRIGING	Min	17.51	23.37	33.95	16.91	22.56	32.78	16.86	22.40	32.62	17.48	23.43	33.94	17.63	23.52	34.17	17.41	23.32	33.80	17.26	23.46	33.61
	Max	17.75	23.68	34.40	18.45	24.62	35.76	18.35	24.58	35.63	17.76	23.61	34.37	17.63	23.53	34.18	17.84	23.73	34.53	17.97	23.68	34.70
	Mean	17.63	23.53	34.17	17.65	23.55	34.21	17.62	23.51	34.15	17.63	23.52	34.17	17.63	23.52	34.17	17.63	23.52	34.17	17.63	23.53	34.17
	SD	0.07	0.09	0.13	0.44	0.59	0.86	0.43	0.63	0.86	0.08	0.05	0.12	0.00	0.00	0.00	0.12	0.12	0.21	0.09	0.03	0.14
RS-HDMR	Min	17.50	23.38	33.93	16.91	22.51	32.77	16.85	22.44	32.61	17.48	23.54	33.94	17.62	23.53	34.14	17.41	23.33	33.80	17.27	23.47	33.62
	Max	17.75	23.70	34.40	18.44	24.56	35.75	18.35	24.63	35.63	17.74	23.54	34.37	17.62	23.54	34.14	17.82	23.73	34.50	18.07	23.75	34.85
	Mean	17.63	23.54	34.17	17.64	23.53	34.19	17.62	23.54	34.15	17.62	23.54	34.16	17.62	23.53	34.14	17.62	23.53	34.16	17.63	23.54	34.16
	SD	0.07	0.09	0.13	0.44	0.59	0.86	0.43	0.63	0.87	0.08	0.00	0.12	0.00	0.00	0.00	0.12	0.12	0.21	0.09	0.03	0.14
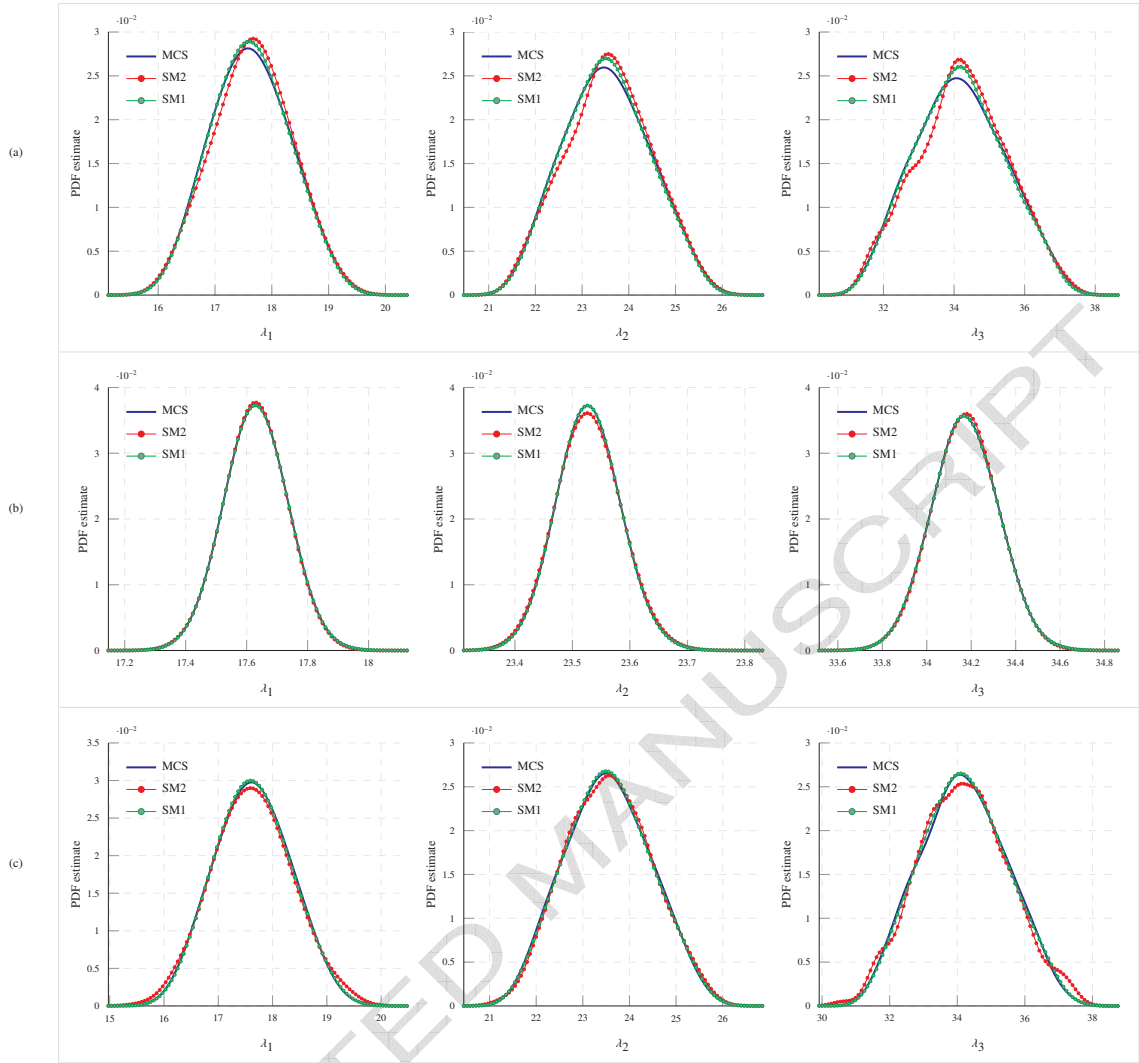
Figure 10: Comparison of the probability density functions (PDF) of the first three natural frequencies of P-FGV CCCC plates obtained by direct MCS (10.000 samples), Kriging (SM1) and RS-HDMR (SM2) metamodels (256 samples). (a) variation of the material parameters with linear reinforcement profile, (b) variation of the reinforcement grading profile and (c) combined variation. ($a/b = 1$, $h/b = 0.1$, $\overline{V}_{CNT}^{*} = 0.11$).
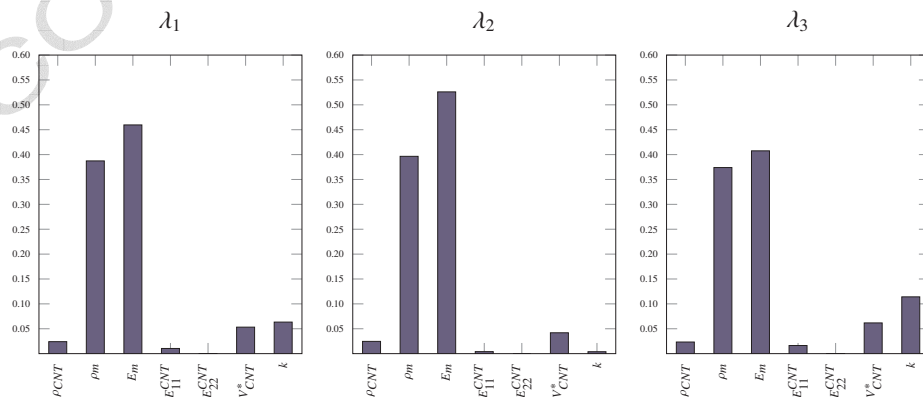

Figure 11: Sensitivity indices with respect to the first three natural frequencies for combined variation of all the variables of CCCC P-FGV plates ($a/b = 1$, $h/b = 0.1$, $\overline{V}_{CNT}^{*} = 0.11$, 256 samples).

18
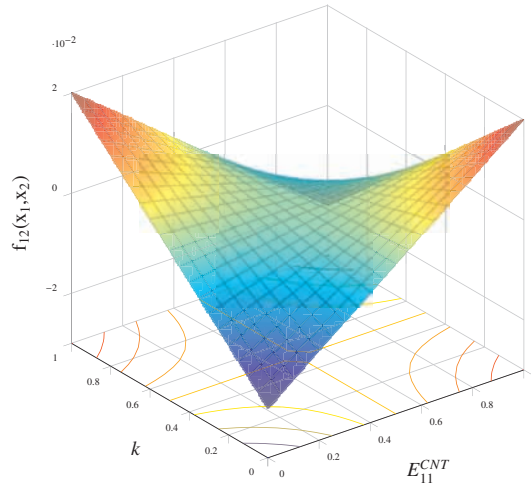
Figure 12: 3D plot for second order component function $f_{12}(x_1, x_2)$ of the response λ_1 with $x_1 = k$ and $x_2 = E_{22}^{CNT}$. (CCCC P-FGV plate, $a/b = 1$, $h/b = 0.1$, $\overline{V}_{CNT}^* = 0.11$, 256 samples).
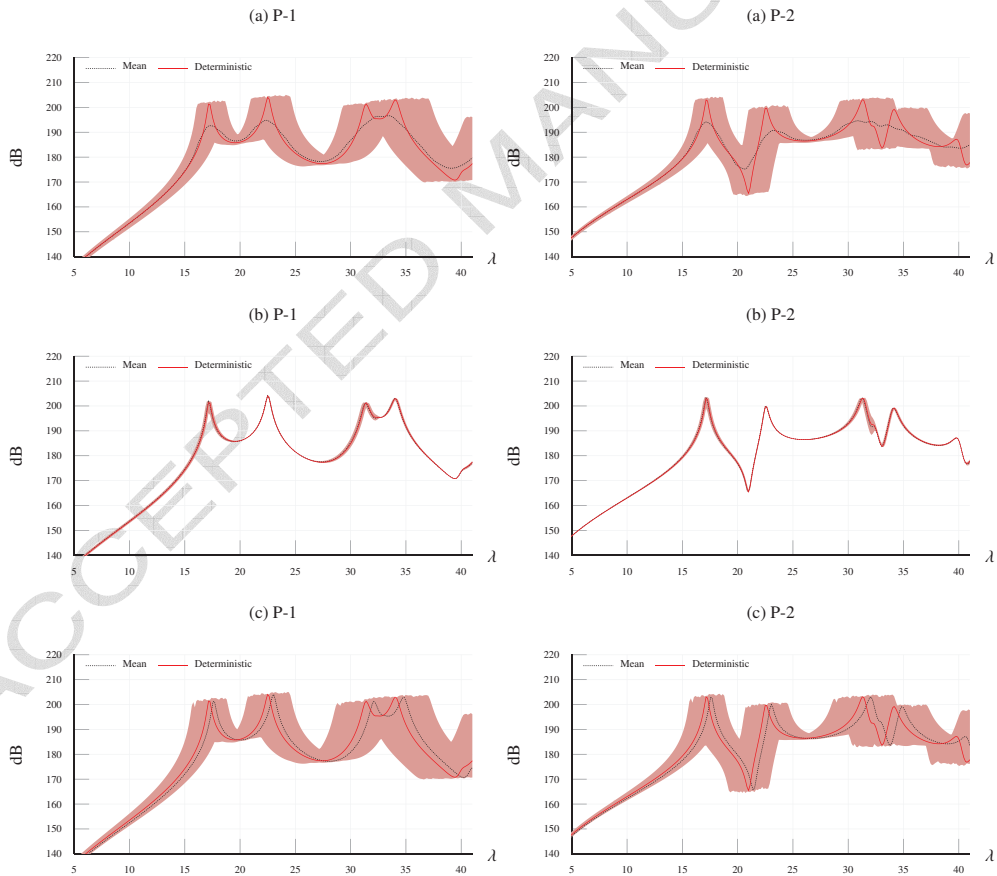

Figure 13: Frequency response function (FRF) plot of simulation bounds, simulation mean and deterministic mean of P-FGV CCCC plates obtained by direct MCS (10.000 samples), Kriging and RS-HDMR metamodels (256 samples). (a) variation of the material parameters with linear reinforcement profile, (b) variation of the reinforcement grading profile and (c) combined variation. ($a/b = 1$, $h/b = 0.1$, $V_{CNT}^* = 0.11$, P-1:{$0.67a, 0.33b$}, P-2:{$0.33a, 0.58b$}, DP:{$0.67a, 0.67b$}).
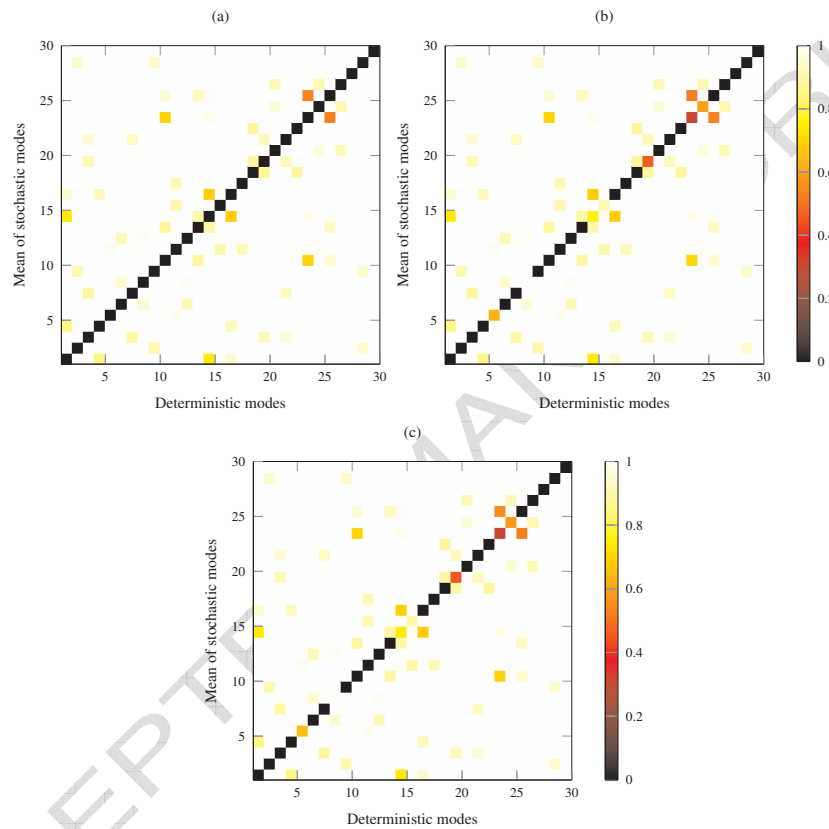
19

Figure 14: 1-MAC matrix comparing the deterministic modes and the mean of the stochastic modes of P-FGV CCCC plates obtained by direct MCS (10.000 samples), Kriging and RS-HDMR metamodels (256 samples). (a) variation of the material parameters with linear reinforcement profile, (b) variation of the reinforcement grading profile and (c) combined variation. ($a/b = 1$, $h/b = 0.1$, $V_{CNT}^* = 0.11$).

6. Conclusions

This article illustrates the influence of randomness in the CNT distribution when acting simultaneously with uncertainty in the CNT/matrix material properties on the vibrational properties of FG-CNTRC plates. The feasibility of applying metamodel-based approaches using Kriging and RS-HDMR is shown in the realm of stochastic analysis. Although the same sampling size as in direct Monte Carlo Simulation (sample size of 10.000) is considered, the number of FE analysis is much less compared to direct MCS and is equal to the number of representative samples (sample size of 256) required to construct the metamodels. It is observed that both metamodels can handle the large number of input parameters. The metamodel formed from a small set of samples is found to establish accuracy and computational efficiency. The results obtained as probability density functions and cumulative distribution functions employing Kriging and RS-HDMR metamodels are compared with the results from direct MCS. It is observed that the matrix parameters have a predominant effect on sensitivity. A significant effect of the power-law index (k) is found on the first and third natural frequencies with considerable contribution from the volume fraction of inclusions (V_{CNT}^*). Interestingly, null sensitivity is identified for the transverse elastic modulus of CNTs (E_{CNT}^*). The volume fraction of CNTs (V_{CNT}^*) is found to hold the maximum sensitivity for the second natural frequency. New dynamic analyses, transient response under impulse loading and the MAC matrix between the mean stochastic and deterministic mode shapes, highlight the propagating effect of the power-law index (k). Process-induced uncertainties in the reinforcement grading profile of FG-CNTRC plates will thus propagate all the sources of uncertainty defined at mid-plane level along the thickness. The key contributions of this study can be summarized as follows:

- The CNT distribution is considered as a source of uncertainty. Power-law distribution functions provide a parametrization of the CNT distribution along the thickness, suitable to characterize uncertainty.

- Metamodel-based approaches using Kriging and RS-HDMR metamodels are shown efficient techniques to evaluate the uncertainty propagation on the vibrational properties of FG-CNTRC plates.

- The power-law index (k) has an important effect on bending stiffness of FG-CNTRC plates. Any uncertainty in the material parameters set up at mid-plane level is propagated along the thickness of the plates by means of the index k.

The future investigation will determine whether the above conclusions hold true for more complex homogenization frameworks.

Acknowledgement

References

[1] S. Iijima, Helical microtubules of graphitic carbon, Nature (London, United Kingdom) 354 (1991) 56–58.

[2] R. F. Gibson, A review of recent research on mechanics of multifunctional composite materials and structures, Composite Structures 92 (2010) 2793–2810.

[3] A. M. Esawi, M. M. Farag, Carbon nanotube reinforced composites: potential and current challenges, Materials & Design 28 (2007) 2394–2401.

[4] A. L. Materazzi, F. Ubertini, A. DAlessandro, Carbon nanotube cement-based transducers for dynamic sensing of strain, Cement and Concrete Composites 37 (2013) 2–11.

[5] T. Schumacher, E. T. Thostenson, Development of structural carbon nanotube–based sensing composites for concrete structures, Journal of Intelligent Material Systems and Structures 25(11) (2013) 1331–1339.

[6] F. Ubertini, A. L. Materazzi, A. DAlessandro, S. Laflamme, Natural frequencies identification of a reinforced concrete beam using carbon nanotube cement-based sensors, Engineering Structures 60 (2014) 265–275.

[7] F. Ubertini, S. Laflamme, H. Ceylan, A. L. Materazzi, G. Cerni, H. Saleem, A. DAlessandro, A. Corradini, Novel nanocomposite technologies for dynamic monitoring of structures: a comparison between cement-based embeddable and soft elastomeric surface sensors, Smart Materials and Structures 23 (2014) 045023.

21

[8] M. S. Konsta-Gdoutos, C. A. Aza, Self sensing carbon nanotube (CNT) and nanofiber (CNF) cementitious composites for real time damage assessment in smart structures, Cement and Concrete Composites 53 (2014) 162–169.

[9] G. Udupa, S. S. Rao, K. Gangadharan, Functionally graded composite materials: An overview, Procedia Materials Science 5 (2014) 1291–1299.

[10] H.-S. Shen, Nonlinear bending of functionally graded carbon nanotube-reinforced composite plates in thermal environments, Composite Structures 91 (2009) 9–19.

[11] P. Zhu, Z. Lei, K. M. Liew, Static and free vibration analyses of carbon nanotube-reinforced composite plates using finite element method with first order shear deformation plate theory, Composite Structures 94 (2012) 1450–1460.

[12] M. Yas, M. Heshmati, Dynamic analysis of functionally graded nanocomposite beams reinforced by randomly oriented carbon nanotube under the action of moving load, Applied Mathematical Modelling 36 (2012) 1371–1394.

[13] M. Heshmati, M. Yas, Vibrations of non-uniform functionally graded MWCNTs-polystyrene nanocomposite beams under action of moving load, Materials & Design 46 (2013) 206–218.

[14] L. Zhang, Z. Song, K. Liew, State-space levy method for vibration analysis of FG-CNT composite plates subjected to in-plane loads based on higher-order shear deformation theory, Composite Structures 134 (2015) 989–1003.

[15] L. Zhang, Z. Lei, K. Liew, Buckling analysis of FG-CNT reinforced composite thick skew plates using an element-free approach, Composites Part B: Engineering 75 (2015) 36–46.

[16] E. García-Macías, R. Castro-Triguero, E. I. S. Flores, M. I. Friswell, R. Gallego, Static and free vibration analysis of functionally graded carbon nanotube reinforced skew plates, Composite Structures (2016).

[17] M. Rouhi, M. Rais-Rohani, Modeling and probabilistic design optimization of a nanofiber-enhanced composite cylinder for buckling, Composite Structures 95 (2013) 346–353.

[18] H. Ghasemi, R. Rafiee, X. Zhuang, J. Muthu, T. Rabczuk, Uncertainties propagation in metamodel-based probabilistic optimization of CNT/polymer composite structure using stochastic multi-scale modeling, Computational Materials Science 85 (2014) 295–305.

[19] G. Li, S.-W. Wang, H. Rabitz, S. Wang, P. Jaff, Global uncertainty assessments by high dimensional model representations (hdmr), Chemical Engineering Science 57 (2002) 4445–4460.

[20] R. Chowdhury, B. Rao, Assessment of high dimensional model representation techniques for reliability analysis, Probabilistic Engineering Mechanics 24 (2009) 100–115.

[21] D. Mukherjee, B. Rao, A. M. Prasad, Global sensitivity analysis of unreinforced masonry structure using high dimensional model representation, Engineering Structures 33 (2011) 1316–1325.

[22] S. Dey, T. Mukhopadhyay, S. Adhikari, Stochastic free vibration analysis of angle-ply composite plates - A RS-HDMR approach, Composite Structures 122 (2015) 526–536.

[23] S. Dey, T. Mukhopadhyay, A. Spickenheuer, S. Adhikari, G. Heinrich, Bottom up surrogate based approach for stochastic frequency response analysis of laminated composite plates, Composite Structures (2016).

[24] S. Dey, T. Mukhopadhyay, S. Sahu, G. Li, H. Rabitz, S. Adhikari, Thermal uncertainty quantification in frequency responses of laminated composite plates, Composites Part B: Engineering 80 (2015) 186–197.

[25] S. Dey, T. Mukhopadhyay, S. Adhikari, Stochastic free vibration analyses of composite doubly curved shells - a Kriging model approach, Composites Part B: Engineering 70 (2015) 99–112.

[26] D.-L. Shi, X.-Q. Feng, Y. Y. Huang, K.-C. Hwang, H. Gao, The effect of nanotube waviness and agglomeration on the elastic property of carbon nanotube-reinforced composites, Journal of Engineering Materials and Technology 126 (2004) 250–257.

[27] J. Fidelus, E. Wiesel, F. Gojny, K. Schulte, H. Wagner, Thermo-mechanical properties of randomly oriented carbon/epoxy nanocomposites, Composites Part A: Applied Science and Manufacturing 36 (2005) 1555–1561.

[28] B. Sobhani Aragh, A. Nasrollah Barati, H. Hedayati, Eshelby-mori-tanaka approach for vibrational behavior of continuously graded carbon nanotube-reinforced cylindrical panels, Composites Part B: Engineering 43 (2012) 1943–1954.

[29] W. M. Helal, D. Shi, Optimum material gradient for functionally graded rectangular plate with the finite element method, Indian Journal of Materials Science 2014 (2014).

[30] G. Wempner, D. Talaslidis, Mechanics of Solids and Shells, CRC Press, 2003.

[31] E. Efraim, M. Eisenberger, Exact vibration analysis of variable thickness thick annular isotropic and fgm plates, Journal of Sound and Vibration 299 (2007) 720–738.

[32] G. Matheron, Principles of geostatistics, Economic geology 58 (1963) 1246–1266.

[33] J. Sacks, W. J. Welch, T. J. Mitchell, H. P. Wynn, Design and analysis of computer experiments, Statistical Science (1989) 409–423.

[34] S. N. Lophaven, H. B. Nielsen, J. Søndergaard, DACE-A Matlab Kriging toolbox, version 2.0, Technical Report, 2002.

[35] J. Koehler, A. Owen, 9 computer experiments, Handbook of statistics 13 (1996) 261–308.

[36] T. J. Mitchell, M. D. Morris, Bayesian design and analysis of computer experiments: two examples, Statistica Sinica 2 (1992) 359–379.

[37] J. Sacks, S. B. Schiller, W. J. Welch, Designs for computer experiments, Technometrics 31 (1989) 41–47.

[38] H. Rabitz, m. F. Ali, General foundations of high-dimensional model representations, Journal of Mathematical Chemistry 25 (1999) 197–233.

[39] G. Li, H. Rabitz, S.-W. Wang, P. G. Georgopoulos, Correlation method for variance reduction of Monte Carlo integration in RS-HDMR, Journal of Computational Chemistry 24 (2003) 277–283.

[40] T. Ziehn, A. Tomlin, GUI-HDMR - a software tool for global sensitivity analysis of complex models, Environmental Modelling & Software 24 (2009) 775–785.

[41] I. M. Sobol, On sensitivity estimation for nonlinear mathematical models, Matematicheskoe Modelirovanie 2 (1990) 112–118.

[42] I. M. Sobol, Global sensitivity indices for nonlinear mathematical models and their Monte Carlo estimates, Mathematics and Computers in Simulation 55 (2001) 271–280.

[43] G. Li, S.-W. Wang, H. Rabitz, Practical approaches to construct RS-HDMR component functions, The Journal of Physical Chemistry A 106 (2002) 8721–8733.

[44] G. Li, H. Rabitz, Ratio control variate method for efficiently determining high-dimensional model representations, Journal of computational chemistry 27 (2006) 1112–1118.

[45] T. Ziehn, A. Tomlin, Global sensitivity analysis of a 3d street canyon model-part i: The development of high dimensional model representations, Atmospheric Environment 42 (2008) 1857–1873.

[46] T. Ziehn, A. S. Tomlin, A global sensitivity study of sulfur chemistry in a premixed methane flame model using HDMR, International Journal of Chemical Kinetics 40 (2008) 742–753.

[47] I. M. Sobol, On the distribution of points in a cube and the approximate evaluation of integrals, USSR Computational mathematics and mathematical physics (1967) 86–112.

[48] Y. Han, J. Elliott, Molecular dynamics simulations of the elastic properties of polymer/carbon nanotube composites, Computational Materials Science 39 (2007) 315–323.

[49] H.-S. Shen, C.-L. Zhang, Thermal buckling and postbuckling behavior of functionally graded carbon nanotube-reinforced composite plates, Materials & Design 31 (2010) 3403–3411.

[50] D. Kammer, L. Yao, Enhancement of on-orbit modal identification of large space structures through sensor placement, Journal of Sound and Vibration 171 (1994) 119–139.